Synthetic model microswimmers near walls

Ketzetzi, S.

Citation

Ketzetzi, S. (2021, June 29). *Synthetic model microswimmers near walls*. *Casimir PhD Series*. Retrieved from https://hdl.handle.net/1887/3185906

Author: Ketzetzi, S.
Title: Synthetic model microswimmers near walls
Issue date: 2021-06-29

6

Self-Propulsion of Symmetric and Asymmetric Dumbbells

Abstract

Biological microswimmers naturally occur in various shapes and forms. Their anisotropic shapes not only enable them to navigate complex biological environments, but have also been predicted to provide them with additional functions, such as viscotaxis and efficient swarming. Despite recent advances, research on synthetic swimmers has so far mostly been limited to spherical shapes and thus little is known about how shape affects motion in such systems. In this chapter, we study the catalytically self-propelled motion of dumbbell-shaped microswimmers near walls. We explore how shape anisotropy affects motion by fully characterizing the motion of dumbbells with different shapes, comprising symmetric, asymmetric and highly asymmetric lobes, for which the driving force is along the short dumbbell axis. We find that increasing particle asymmetry leads to circular motion. Particles move at similar translational speeds, while their angular speeds increase with particle asymmetry. In addition, we measure and compare the radius of particle trajectories to existing theory on asymmetric self-propelled particles near a wall. The good agreement that we find confirms that the radius of circular motion depends on particle shape and coating. Our findings advance the understanding of anisotropic microswimmer self-propulsion near walls and, in turn, may prove useful for increasing swimming efficiency, directionality, and motion control in patterned environments.

Introduction

Shape and motion are profoundly interconnected on the microscale. Actively self-propelled microspheres typically move in straight trajectories before their motion becomes randomized due to thermal noise. At elevated densities, such spheres [26, 44, 198] are known to exhibit activity-induced phase separation into dilute gas-like phases and dense highly dynamic cluster phases. Simulations predict that departure from the ideal spherical shape can result in various types of motions, which are hypothesized to aid in achieving precise motion control or even provide novel functionalities. For example, simulations show that by breaking swimmer symmetry, circular trajectories [84] and spiral [279] or chiral-type [280] trajectories can be obtained in two and three dimensions, respectively. In the case of particles that are asymmetric with respect to their propulsion direction, the propulsion force is predicted to lead to a velocity-dependent torque relative to the particle center-of-mass, due to a coupling between translational and orientational motion [84]. Moreover, swimmers that have non-uniaxial shapes are predicted to experience aligning torques, for example in viscosity gradients, showing that tactic behaviors may be obtained without the need for energy-consuming mechanisms [281]. Anisotropic shapes are also expected to influence swimmer interactions and collective swimmer behavior [280, 282]: for instance, torques on anisotropic swimmers are expected to influence activity-induced phase separation in active dumbbells [283] and rods [284]. Hence, answering how symmetry and shape couple to motility and motion patterns is important for understanding and ultimately controlling the behavior of single as well as collections of swimmers.

Nowadays, nonspherical swimmer shapes such as dumbbells and rods can be obtained in the laboratory through chemical synthesis, or even as we demonstrated recently [88], through 3D microprinting which allows for further flexibility in particle shape and in choosing the location of the active site on the particle. Thus, the aforementioned predictions from simulations can readily be tested in experiments employing synthetic model swimmers of nonspherical shapes.

Already, the limited number of studies on shape-dependent motion of synthetic particles have provided interesting insights into the effect of shape: 10-µm-long L-shaped particles in critical binary solvents exhibited circular trajectories near a wall upon light illumination, in agreement with predictions [84]. Along the same line, experiments on straight and bent electrophoretic microrods showed that trajectories changed from straight to circular when the particle shape changed from a straight to an L-shaped rod [85], while experiments on chemically propelled half-spheres showed a transition from straight to circular motion, in addition to changes in the particle orientation with respect to the wall with increasing fuel concentration [87]. Chemically propelled prolate ellipsoids showed a transition from 3-dimensional passive Brownian motion at low fuel concentration to 2-dimensional active motion at intermediate fuel concentration and even spinning at high fuel concentration [86]. In addition, particle speed increased with ellipsoid length [86]. More recently, helical particles were found to swim slightly faster than spheres of the same cross-section and material, possibly due to the shape-induced coupling between translation along and rotation around their long axis in combination with the propulsion force that increased their rotation [88]. Finally, chemically propelled asymmetric dumbbells — with the smaller lobe being the catalyst — showed both quasi-linear as well as quasi-circular trajectories, and an increase in speed when increasing the size of the catalytic lobe [285]. However, in these experiments dumbbells were formed by sputtering Pt layers on silica spheres. These were subsequently annealed so that the Pt layer de-wet, thereby forming a sphere-like Pt particle attached onto the silica. Consequently, the size and shape of the catalytic site was highly irregular, especially when increasing the catalyst site size. Hence, to pinpoint the effect of shape on active motion, controlled experiments in which the shape is preserved while the degree of asymmetry with respect to the propulsion direction varies are highly desirable.

Here, we employ chemically synthesized symmetric and asymmetric dumbbell-shaped swimmers with well-defined shapes to gain insight into how shape contributes to the active motion. To this end, we experimentally study and fully characterize their catalytically propelled 2-dimensional motion near a wall. We find that increasing particle asymmetry leads to pronounced circular motions. Surprisingly, particles move at similar translational speeds, while their angular speeds strongly increase with particle asymmetry. We directly measured the radius of particle trajectories and, subsequently, compared our measurements to theory [84], which predicts that the radius of circular motion for asymmetric particles self-propelled near a wall solely depends on the diffusional properties of the particles determined by their shape, finding good agreement.

Results and Discussion

Through chemical synthesis, we prepared dumbbell-shaped particles with three different aspect ratios α — the ratio between the size of the larger lobe and the smaller lobe — by creating protrusions on polystyrene spheres following the method of Ref. [286]. That is, we prepared symmetric ($\alpha = 1.03 \pm 0.03$), asymmetric ($\alpha = 1.6 \pm 0.1$), and highly asymmetric dumbbells ($\alpha = 2.7 \pm 0.4$). In brief, we started from the same sphere batch of seeds and created three

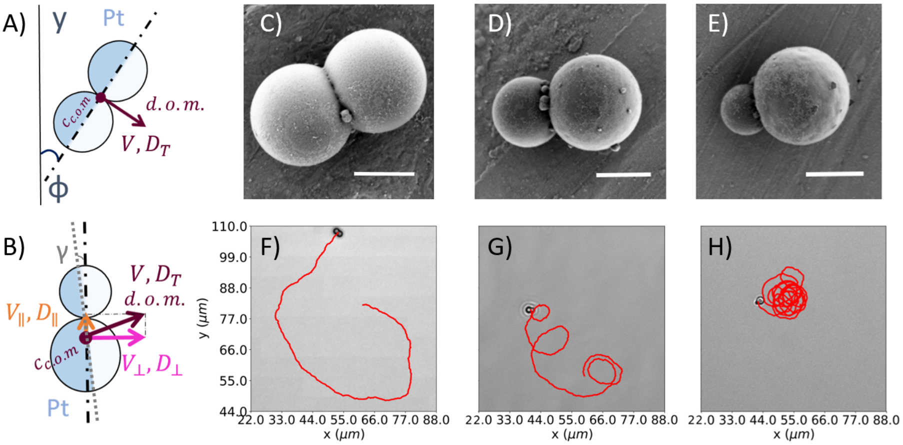

Figure 6.1: **Self-propelled motion of symmetric and asymmetric dumbbells moving in two dimensions above a wall. A-B)** Schematic representation of the motion: all dumbbells are half-coated with (4.8 ± 0.2) nm Pt. Their direction of motion, $d.o.m.$, is always away from their coating. We are interested in studying the velocity, V, and translational diffusion coefficient, D, of the dumbbell center-of-mass, $c_{c.o.m.}$. **A)** For a perfectly symmetric dumbbell with a symmetric coating, the Pt coating and hence the $d.o.m.$ is aligned perpendicular to the long dumbbell axis, see dashed line, due to the preparation method. **B)** For an asymmetric dumbbell, the coating is slightly asymmetric and forms an angle γ with respect to the dumbbell long axis, hence the $d.o.m.$ is not expected to be exactly perpendicular to its long axis. We additionally measure the motion parallel ($V_\parallel, D_\parallel$) and perpendicular ($V_\perp, D_\perp$) to the long dumbbell axis by projecting the displacement of its center-of-mass in the two directions, see orange and magenta vectors, respectively. The same holds for symmetric particles that are not perfectly half-coated: asymmetry in the coating will result in motion that deviates from the perpendicular to the long axis direction. **C-E)** SEM images of dumbbells with different aspect ratios, α, obtained via chemical synthesis and subsequent half-coating with Pt. The brighter particle sides indicate the coating. Scale bars are 1 μm. **C)** Symmetric dumbbells ($\alpha = 1.03 \pm 0.03$). **D)** Asymmetric dumbbells ($\alpha = 1.6 \pm 0.1$). **E)** Highly asymmetric dumbbells ($\alpha = 2.7 \pm 0.4$). **F-H)** Shape-dependent particle trajectories. A bright field image of the final position of each dumbbell is superimposed on its trajectory. The dimensions of the field of view in the microscopy images are the same. **F)** Symmetric dumbbells move in open straight trajectories, randomized by thermally induced changes in direction. Image shows a 21 s trajectory, $V = (7.2 \pm 2.1)$ μm/s, before leaving the field of view. **G)** Asymmetric dumbbells move in quasi-circular trajectories. Image shows a 25 s trajectory, $V = (7.3 \pm 2.0)$ μm/s. **H)** Highly asymmetric dumbbells move in circular trajectories. Image shows a 25 s trajectory, $V = (8.3 \pm 2.6)$ μm/s.

dumbbell batches with different sizes in their protruded spheres. The lobe sizes were (1.74±0.05) and (1.69±0.04) µm for the symmetric, (1.59±0.07) and (1.00±0.05) µm for the asymmetric, and (1.56±0.07) and (0.59±0.08) µm for the highly asymmetric dumbbells, as measured from scanning electron microscopy (SEM) images. Details on dumbbell preparation are provided in the Methods. Subsequently, we sputter coated all dumbbells from above with a (4.8±0.2) nm thick Pt coating while they laid flat on glass substrates, i.e., we half-coated the dumbbells along their long-axis direction (see Figures 6.1A-B for a schematic and Figures 6.1C-E for example SEM images). As all dumbbells laid flat on the substrate during the coating procedure, for an asymmetric dumbbell we expect, due to the size asymmetry between its two lobes, that the Pt coating will be positioned at an angle with respect to its long axis, see γ angle in Figure 6.1B. From the size ratios, we calculated γ to be 3^o, 13^o, and 27^o for the symmetric, asymmetric, and highly asymmetric dumbbells, respectively.

To investigate the effect of shape asymmetry on self-propelled motion, we dispersed all dumbbells in 10% aqueous H_2O_2. The particles quickly sedimented to the glass substrates. We recorded their two-dimensional motion, in the direction away from their long axis, after settling above the substrate, and subsequently analyzed their motion using python routines. We found that the self-propelled trajectories depended on dumbbell morphology, see Figures 6.1E-G. Symmetric dumbbells, with $\alpha \approx 1$ as in Figure 6.1C, tended to move in straight lines at short times, see Figure 6.1F, while their motion became random at longer times due to thermal noise. Over similar timescales, particles that were asymmetric with respect to their propulsion direction, see Figures 6.1D and 6.1E, exhibited circular motion. The circularity in the trajectories became more pronounced with increasing particle asymmetry, with the highly asymmetric dumbbells typically moving in small consecutive circles, see Figures 6.1G and 6.1H for dumbbells with $\alpha \approx 1.6$ and $\alpha \approx 2.7$, respectively.

We wished to investigate whether theoretical predictions on the circularity of asymmetric particle trajectories hold for our catalytic dumbbells of different shapes near a wall. To this end, we characterized the particles' motion as a function of dumbbell shape, see Methods for details on motion analysis. First, we examined the translational components of the motion, i.e. the translational velocity, V, and diffusion coefficient, D_T. These parameters were obtained from fitting the mean-squared displacement of the dumbbell center-of-mass, determined with the software package trackpy, with $\Delta r^2 = 4D\Delta t + V^2\Delta t^2$ using the method of Ref. [30]. Surprisingly, we found that V remained rather constant with increasing aspect ratio α in Figure 6.3A. This constancy is initially unexpected, based on the well-known speed decrease of spherical particles with size [58, 157], since the overall size here decreases with increasing aspect ratio.

However, at the same time, the larger, symmetric, dumbbells have a larger surface area covered by the Pt which may compensate for the similarity in particle speeds. We also found that the translational diffusion coefficient D_T increased with α as shown in Figure 6.2D.

Due to asymmetries in either the metal coating or the dumbbell shape, motion of the dumbbell center-of-mass will slightly deviate from the motion perpendicular to the dumbbell long axis direction, as shown in the schematic of Figure 6.1B. Therefore, to gain further insight in dumbbell self-propulsion, the displacement vector of the center-of-mass is projected parallel and perpendicular to the dumbbell long axis yielding the center-of-mass displacements in the respective directions, see the orange and magenta vectors in Figure 6.1B. The parallel and perpendicular mean-squared displacements were then calculated from the respective displacements in time. By doing so, we obtained the motion parameters $(V_\perp, D_\perp)$ and $(V_\|, D_\|)$ in the parallel and perpendicular directions from parallel and perpendicular mean-squared displacement fits [30]. As in the translation speeds V, we find that the perpendicular speeds are, within error, similar for all shapes, see Figure 6.2B. Since this direction typically coincides with the direction of propulsion, this suggests that the propulsion force is also similar, in spite of the difference in dumbbell sizes and coating surface coverage. In the parallel direction, however, speed increases with aspect ratio in Figure 6.2C. The diffusion coefficients in the perpendicular, $D_\perp$, and parallel directions, $D_\|$ are shown in Figures 6.2E and 6.2F, respectively.

In contrast to the shape-independent translational velocity, the angular velocity, ω, strongly increases with aspect ratio, see Figure 6.2G. In addition, we find that the timescale for rotation, τ_R, obtained from the rotational diffusion coefficient, D_R, via $\tau_R = 1/D_R$, strongly decreases with aspect ratio, see Figure 6.2H. The rotational parameters ω and D_R were obtained from fitting the mean-squared angular displacement of the dumbbell following Ref. [83]. For the angular displacement, we considered the angle ϕ, defined as in Figure 6.1A. That is, we calculated the angle between the long axis of the dumbbell and a fixed angle in the laboratory frame — y axis — in time. To obtain a quantitative relation between translational and rotational velocity, we plotted V as a function of ω for individual dumbbells of each shape in Figure 6.2I. The dashed lines represent least-squares fits with $y = \beta x$. We find that the slope of the curves, which can be interpreted as a measure of curvature of the particle trajectories, decreases with aspect ratio: the respective slope, β, for the symmetric (blue), asymmetric (red) and highly asymmetric (black) dumbbells is (74 ± 11) µm, (28 ± 4) µm, and (17 ± 2) µm.

We furthermore examined the orientation of the self-propelled dumbbells, θ, in

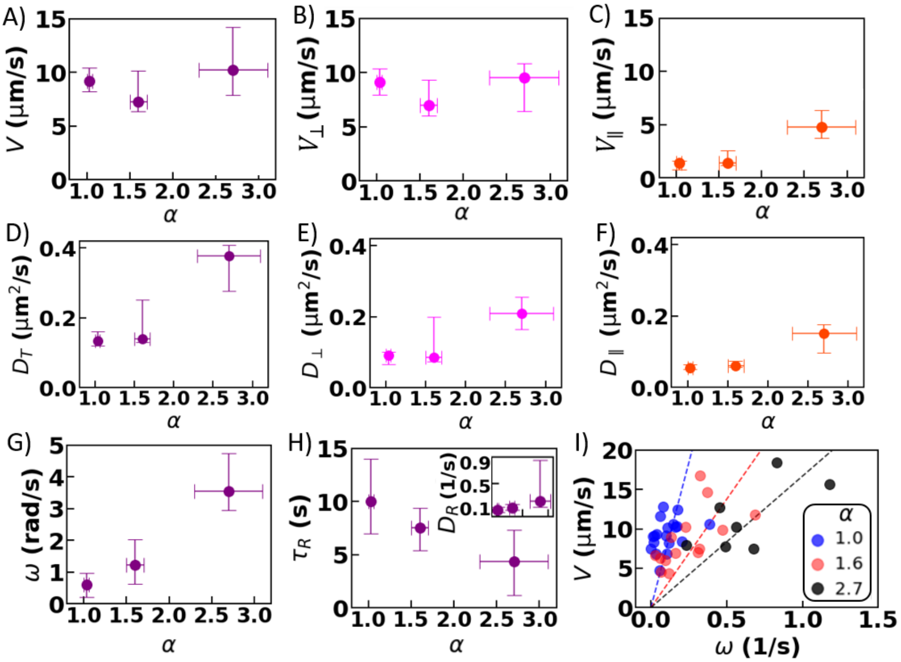

Figure 6.2: **Translational and rotational self-propelled dumbbell motion.** A-H) Dumbbell properties as function of the aspect ratio, α. Each reported value is the median of averaged values obtained from individual particles of the same α, the errors reporting first quartiles. **A)** Translational velocity, V. **B)** Translational velocity perpendicular to the dumbbell long axis, $V_{\perp}$. **C)** Translational velocity parallel to the long axis $V_{\parallel}$. **D)** Translational diffusion coefficient, D_T. **E)** Translational diffusion coefficient perpendicular to the dumbbell long axis, $D_{\perp}$. **F)** Translational diffusion coefficient parallel to the dumbbell long axis, $D_{\parallel}$. For definitions of all the above parameters see Figure 6.1B. **G)** Angular velocity, ω, obtained following Ref. [83] by fitting the mean-square angular displacement of ϕ, the angle between the dumbbell long axis and a fixed axis in the microscope frame, see Figure 6.1A for a schematic. **H)** Timescale for rotation, τ_R (main), and rotational diffusion coefficient, D_R (inset), with D_R obtained as described in (G). **I)** Translational velocity plotted against angular velocity, with the color denoting the aspect ratio. Each data point shows average values that correspond to an individual particle. Dashed lines are least-squares fits with $y = \beta x$, with β (74 ± 11) µm (blue), (28 ± 4) µm (red), and (17 ± 2) µm (black).

the particle-centered frame by considering the angle between the displacement vector of the dumbbell center-of-mass $\Delta\mathbf{r}$ in consecutive frames (d.o.m.) and the perpendicular component of the velocity, see Figure 6.3A. For a symmetric dumbbell and symmetric coating we expect the two vectors to coincide, i.e. θ to be zero. The θ values that we obtain for symmetric dumbbells that move in straight trajectories, are indeed close to 0^o, while θ increases with aspect ratio, see Figure 6.3B, as expected from particle trajectories. We notice that for the symmetric and asymmetric dumbbells these angle values are similar to the calculated γ angles between the long and the Pt coating axes (see also Figure 6.1), while for the highly asymmetric dumbbells θ is higher than γ. If the apparent difference in direction of motion from the perpendicular orientation would solely stem from the asymmetric coating, we would expect that $\theta = \gamma$. However, the observed difference in Figure 6.3B, suggests that particle shape also contributes to the angular motion. Moreover, we find that θ increases with the angular particle velocity in Figure 6.3C. However, we note that translational velocity is unaffected by the orientation of the dumbbell in the particle-centered frame (Figure 6.3D).

Lastly, we study the average local curvature, LC, of particle trajectories, see Methods for details on trajectory characterization using a Savitzky Golay filter that performs polynomial curve fits to smoothen out the noise. We find that LC increases with increasing aspect ratio in Figure 6.4A, in line with our observations on particle trajectories shifting from straight to circular with increasing dumbbell asymmetry, see Figure 6.1. We additionally obtain the radius, R with $R = \frac{1}{LC}$, of particle trajectories from the average curvature values that we determined. We found that the radius of the trajectory decreases with the dumbbell

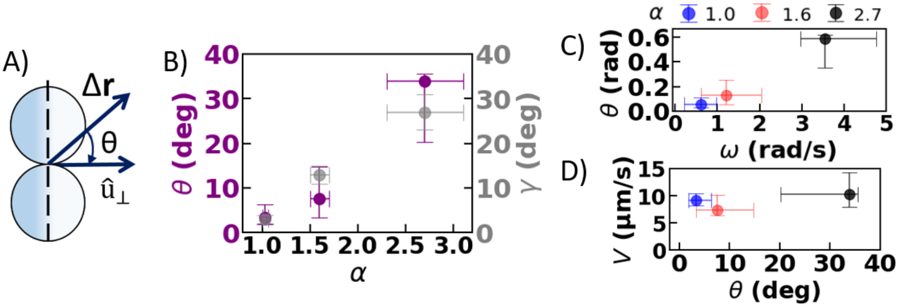

Figure 6.3: **Orientation of self-propelled dumbbells. A)** The orientation in the particle frame, θ, is the angle between the normal vector of the dumbbell long axis, and the displacement vector. **B)** Orientation θ as a function of aspect ratio, α. **C)** Orientation θ, as function of angular velocity, ω. **D)** Translational velocity, V, as function of θ. All values reported here are medians of averaged values obtained from individual particles of the same α, the errors report first quartiles.

angular velocity in Figure 6.4B. Note that the translational velocity remains unaffected by the radius of the trajectory in Figure 6.4C.

We directly compare our findings for the radius with the theoretical prediction for the radius of asymmetric particles from Ref. [84]. By taking into account the presence of a substrate using the Stokeslet close to a no-slip boundary to model the hydrodymanic interactions, Ref. [84] showed that instead of using the generalized mobility tensor for bulk motion [287], the radius of the parti-

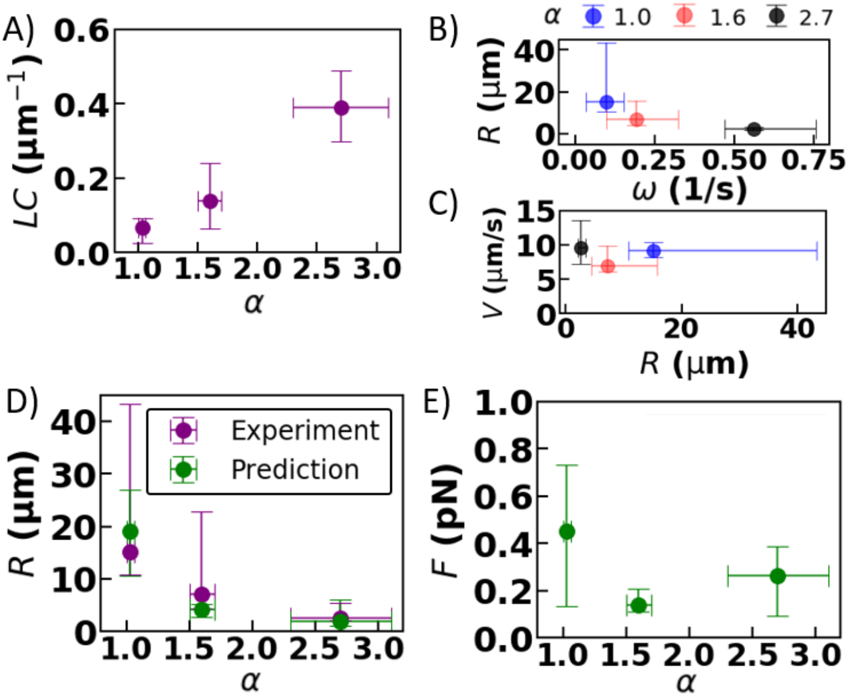

Figure 6.4: **Characterizing the trajectory of self-propelled dumbbells: local curvature and radius.** **A)** Average local curvature, LC, as function of aspect ratio, α. **B)** Radius of trajectory, R, with $R = 1/LC$, as function of angular velocity, ω. **C)** Translational velocity, V, as function of R. **D)** R with α, as measured from our experiments (purple) and as obtained using theory (green) [84]. **E)** Effective propulsion force, F, with α, for our dumbbells calculated using the theory of Ref. [84] and experimentally measured values for ω, D_R, and ℓ. All values reported here are medians of averaged values obtained from individual particles of the same α, errors report first quartiles.

cle trajectory near a wall may be obtained with the expression $R = |\frac{D_\perp}{\ell D_R}|$, where ℓ is the length difference between the middle of the metal coating axis and the particle center-of-mass projected on the long axis. We, thus, used this expression to calculate the predicted radius that corresponds to our dumbbells with different aspect ratios from our measured values of $D_\perp$ and D_R, see insets of Figures 6.2E and 6.2H, respectively. For the ℓ parameter, we used 0.05 µm (symmetric), 0.20 µm (asymmetric), and 0.27 µm (highly asymmetric dumbbells). These approximate values were obtained from the distance difference between the middle of the long axis of our dumbbells, the length of which was determined from SEM images, and the dumbbell center-of-mass position, see Methods for center-of-mass determination. We found a good agreement between the measured (purple points) and the predicted values (green points) for the radius in Figure 6.4D. Finally, we calculated the effective propulsion force for dumbbells of different shapes. According to Ref. [84], the force, F, near the wall is given by $F = \frac{k_B T \omega}{D_R \ell}$. By employing ω and D_R values shown in Figures 6.2G and 6.2H, respectively, and ℓ values mentioned above, we found that the propulsion force is ≈ 0.1 pN (Figure 6.4E). Together, these findings confirm the expectation that the radius of trajectory depends on particle shape, while it is independent of propulsion strength [84], although the latter is surprising due to differences in dumbbell size and Pt surface coverage.

Conclusions

We examined the motion of self-propelled dumbbells with different aspect ratios, from highly symmetric to highly asymmetric shapes. We found clear differences in dumbbell motion, which switched from straight to circular with increasing particle asymmetry, due to their asymmetric shape and coating. By fully quantifying their motion properties, we discovered that although our dumbbells propel themselves with similar translational velocity, their angular velocity strongly increases with particle asymmetry. We further measured the local curvature and corresponding radii of their trajectories, and found that the radius strongly decreases with particle asymmetry in line with our observations. Most importantly, the radii that we measured were in good agreement with theoretical predictions on asymmetric particles moving near a wall.

According to theory, the translational and rotational motion of asymmetric particles are coupled under an intrinsic force that sets the speed [84], while, due to the anisotropic shape, an additional velocity-dependent torque is generated. Our measurements on differently shaped particles, confirmed that the radius of circular motion depends on particle shape and coating [84], while it does not depend on propulsion strength. However, that propulsion strength remained roughly the same for all considered shapes, i.e. sizes and metal surface coverage, contrasts spherical particle behaviors for which propulsion strength is found to depend on these parameters.

Overall, our findings showed that departure from the spherical shape, predominantly used in microswimmer studies, leads to significant effects on the active motion on the individual particle level. The dumbbell shapes used here may prove to be of great interest, because although they are considerably more complex than spheres, they can be modelled in simulations. A future comparison to simulations can aid in predicting their collective behavior, typically remaining experimentally largely unexplored due to limitations in fuel consumption.

Acknowledgements

I thank Rachel Doherty for synthesizing the dumbbell particles of different aspect ratios studied in this chapter and for scanning electron microscopy imaging, and my student Ivar Schrëtlen for developing python routines and for performing data analysis on dumbbell motion.

Methods

Dumbbell synthesis. First, linear polystyrene (PS) spheres were synthesized by a dispersion polymerization method and crosslinked by the addition of a swelling solution containing 90:10 v:v styrene:TPM, 1.5% v/v divinylbenzene (DVB) and 2 wt% azobisisobutyronitrile (AIBN), following the protocol of Ref. [288]. Subsequently, to form the dumbbells, protrusions were created on the spheres following the method of Ref. [286]. Here, 25 mg of AIBN and 0.567 ml of 0.5% aqueous hydroquinone (HQ) were added to 3.5 ml of aqueous 2 wt% solution of poly(vinyl alcohol) (PVA) and a variable amount of monomer solution consisting of 90:10 v:v styrene:TPM. This mixture was then emulsified at 8,000 rpm for 2 min and 10,000 rpm for 30 s using an IKA Ultra-Turrax disperser. 1.5 ml of 4.9 wt% crosslinked PS was added to this emulsion while vortexing. The emulsion was bubbled with N_2 for 20 s, sealed, and rotated in the dark for 24 h. After this second swelling step, the emulsion was heated while rotating in an oil bath at 80 deg for 24 h. The size of the protrusion, and thereby the dumbbell, was controlled by controlling the swelling ratio, which is defined as the mass of the added monomer divided by the mass of the polymer colloids. The swelling ratios for the three different batches used here were 1.25, 1.5 and 2.75. The dumbbells in the resulting particle batches had a long axis of (2.2 ±

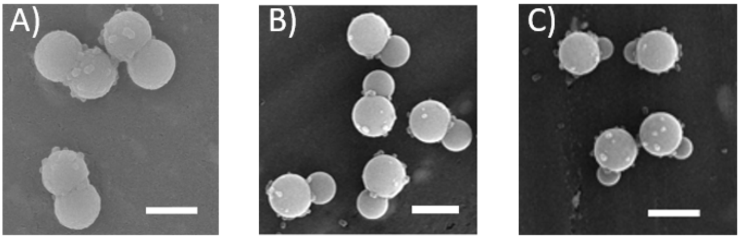

Figure 6.5: Scanning electron microscopy images of synthesized dumbbell particles, also used for particle characterization. Scale bars are 2 µm.

0.1) µm, (2.6 ± 0.1) µm, and (3.1 ± 0.1) µm, respectively, with the corresponding aspect ratios — i.e. size of the larger lobe divided by the size of the smaller lobe — being (2.7 ± 0.4), (1.6 ± 0.1), and (1.03 ± 0.03), respectively. The batch sizes and corresponding aspect ratios were measured from SEM images by sizing 27, 25, and 23 particles, respectively, see Figure 6.5 for examples.

Preparation of Pt-coated dumbbells. To prepare Pt-coated particles, we followed the same procedure as in the previous chapters, which — briefly — requires drying the particles on glass slides, sputter-coating with Pt, and redispersion in water using ultrasonication. Here, the drying process prior to Pt-coating application on the glass, in combination with the redispersion step, initially lead to adsorption and deformation of the PS/TPM dumbbell surfaces as well as to large Pt flakes being released in the samples during redispersion. We therefore took additional steps to ensure that dumbbell surfaces remained smooth at all times, and that the Pt was properly adhered on the dumbbells while it remained on the glass during redispersion. The first step was to clean the dumbbell surfaces by washing them thoroughly (x6) in MilliQ (MQ) water. The second step was to treat the glass slides on which the dumbbells were deposited, prior to Pt coating. For this, we followed a protocol from Ref. [289]: the slides were successively immersed for 1 min in six separate containers with 1 M aqueous KOH, MQ, 1% w/w aqueous poly(ethyleneimine), MQ, 1% w/w aqueous poly(styrenesulfonate) salt, and MQ. To remove excess polymer and salt, they were then cleaned (x6) in MQ and subsequently placed in MQ for 10 min, and dried with N_2. Dumbbells were subsequently either spin coated, or drop-casted and spread, from ethanol dispersions on the treated slides. To ensure a homogeneous Pt coating, we inspected proper spreading of particles on the glass slide for each batch. To ensure proper adhesion when applying the Pt coating with a Cressington sputter-coater, we first sputter coated from above a thin layer of (0.6 ± 0.2) nm of Chromium, followed by (4.8 ± 0.2) nm of Pt/Pd (80:20), while rotating the flat stage with the slides, for even Pt distribution across the slides.

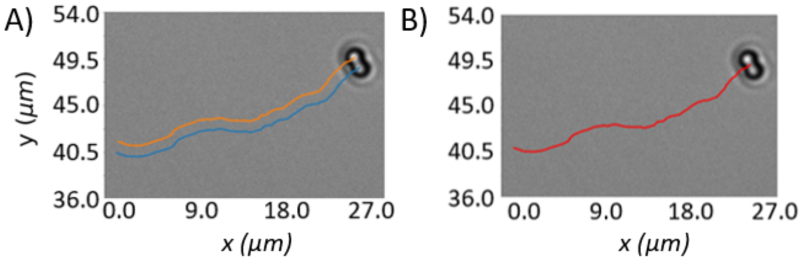

Figure 6.6: **Example of the two-step process performed to track the dumbbells under study.** **A)** The trajectories of the two lobes of the dumbbell particle over 50 frames (≈ 2.6 s) of a symmetric dumbbell are shown in blue and orange. A light microscopy image of the dumbbell is superimposed at 0 s. **B)** The trajectory of the center-of-mass of the same dumbbell as in (A) during the same frames, shown in red. A light microscopy image of the dumbbell is also superimposed.

After these steps, the Pt-coated dumbbells, see Figure 6.1 as an example, were removed from the slides and redispersed in water by ≈ 15 min sonication. The colloids were subsequently washed and stored in water.

Imaging. Pt-coated dumbbells were dispersed in 10% aqueous H_2O_2 at dilute particle concentration. Their motion was recorded with an inverted Nikon Eclipse Ti microscope equipped with a 60x long working distance objective (S Plan Fluor ELWD, NA 0.7) and/or an 100x oil objective (APO TIRF, NA 1.49) above glass cover slips. Cover slips were purchased from VWR and used as received. For the highly asymmetric dumbbells whose imaging required a higher magnification, the zoom 1.5x setting was used (0.06 μm/px). Movies were acquired in the xy-plane at a frame rate of 19 fps typically for 25 s. For the symmetric dumbbells which tend to move in straight lines, movie duration is sometimes shorter due to them leaving the field of view. Measurements were performed in the dark and typically within the hour after sample preparation.

Tracking. Tracking was performed using Trackpy [141]. First, the two spheres comprising the dumbbells were located for each frame, and the individual sphere positions were linked in time, see Figure 6.6A. For the asymmetric dumbbells, the parameters used for tracking their comprising spheres were different, due to the different sphere sizes. The sphere locations were then used to track the center-of-mass of the dumbbell throughout the measurement, see Figure 6.6B, which due to symmetry is always located on the line that passes through the centers of the separate spheres. To determine the center-of-mass position, $c_{c.o.m.}$, the average position of the two spheres was used for the symmetric dumbbells, while for the asymmetric dumbbells the expression $c_{c.o.m.} = \frac{m_{Sm}c_{Sm}+m_B c_B}{m_{Sm}+m_B}$ with m the sphere mass and c the position of the sphere center, was used. Subscripts "Sm" and "B" denote the small and big sphere, respectively. For similar sphere mass density, $\frac{m_{Sm}}{m_B} = (\frac{r_{Sm}}{r_B})^3$, with r the sphere radius, and thus, $c_{c.o.m.} = \frac{c_{Sm}A^3+c_B}{A^3+1}$ with $A = r_{Sm}/r_B$.

Translational and angular velocity. After calculating the center-of-mass position in time as discussed above, we subsequently calculated the mean square displacement of the center-of-mass of the dumbbell. Its translational velocity and corresponding diffusion coefficient was subsequently calculated by fitting its short-term mean-square displacement (MSD) up to $\approx$ 0.2 s [30]. We cross-checked that the time derivative of the displacement method employed in chapter 4 yielded similar results, with the average velocity value obtained from the MSD method being lower by 4%, due to the MSDs containing additional information about the passive component of particle motion. To determine the angular velocity, ω, of the particles, we first extracted the orientational coordinate, ϕ, as function of time from our movies, and subsequently calculated and analyzed the mean-square angular displacement (MSAD, $\Delta\phi^2(t)$) that we obtained from Trackpy, using the Langevin description of Ref. [83]. That is, we performed a least-squares fit of the MSAD with $\Delta\phi^2(t) = 2D_R t + \omega^2 t^2$, where D_R is the rotational diffusion coefficient. From D_R we additionally obtained the rotational diffusion time, τ_R, via $\tau_R = 1/D_R$. Here, the angle ϕ in each frame is the angle between the vector that goes through the long axis of the dumbbell, and a fixed vector aligned with the reference vector (y-axis) of the microscope frame, i.e. ϕ describes the dumbbell orientation in the laboratory frame.

Local curvature of the trajectory. The (local) curvature between two points S_1 and S_2, with both points being the position of the dumbbell center-of-mass in consecutive frames, see Figure 6.7A for a schematic, is obtained by dividing the angular difference $d\beta$ between the tangent lines of points S_1 and S_2 by the path length of the curve between the two points; following Ref. [290], the curvature is calculated using the expression $LC = \frac{d\beta}{dS} = \frac{x'y'-y'x''}{(x'^2+y'^2)^{3/2}}$. The prime in this expression denotes derivation with respect to time, thus the velocity and acceleration of the center-of-mass is calculated in the x and y directions for each frame. For a straight trajectory, LC between the points along the trajectory is zero. An example center-of-mass trajectory of an asymmetric dumbbell and the corresponding LC calculated with the above expression are shown in the top panels of Figures 6.7B and 6.7C, respectively. Due to the dumbbell trajectories being influenced by Brownian motion, the resulting LC data are noisy. We thus filter out the effects of the noise by applying a Savitzky-Golay filter, see Ref. [291, 292], on the trajectory and repeat the LC calculation. The filter smoothens the data without

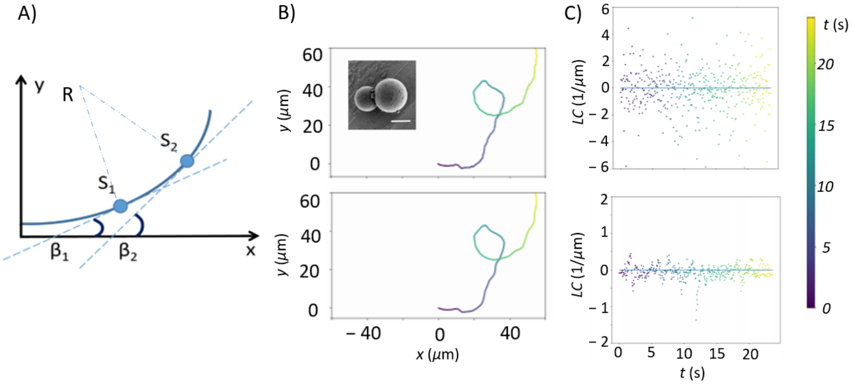

Figure 6.7: **Local curvature determination and application of Savitzky Golay (SG) filter on dumbbell trajectory. A)** The local curvature between two points along the center-of-mass trajectory is obtained from the angular difference ($\beta_2 - \beta_1$) between the tangent lines of the two points divided by the path length ($S_2 - S_1$). **B)** Trajectory without (top) and with (bottom) the SG filter of an asymmetric dumbbell (inset). **C)** Local curvature without (top) and with (bottom) the SG filter for the same dumbbell as in (B). The data in (B, C) is colorcoded with respect to time (in s) after the beginning of the measurement.

disturbing the underlying signal, see the bottom panels of Figures 6.7B and 6.7C for the filtered trajectory and corresponding LC values for the same trajectory as in the top panel. Filtering is achieved using built-in functions in python, which perform least-squares fits of a low order polynomial through subsets of the data (windows) to smoothen the dataset: the local polynomial function is fitted to the input data in the window, and a new replacement data point is calculated using the polynomial function; the process repeats for all windows.